AIAA JOURNAL
Vol. 39, No. 4, April 2001

Numerical Analysis of Dynamic Stability of a Reentry Capsule at Transonic Speeds

Susumu Teramoto,* Kouju Hiraki,† and Kozo Fujii‡
Institute of Space and Astronautical Science, Sagamihara, Kanagawa 229-8510, Japan

Dynamic stability of a reentry capsule in transonic speeds is discussed. An unsteady flowfield around the capsule under the forced pitching oscillation in the transonic flow of $M = 1.3$ is numerically simulated based on the three-dimensional thin-layer Navier–Stokes equations. The numerical result reveals that the dynamic instability is caused by the phase delay of the base pressure. It is also found that the base pressure, the recompression shock wave, and the wake behind the recompression shock wave all oscillate with the same delay time. The flow mechanism is proposed based on the idea that the phase delay of the base pressure is caused by a feedback loop of the flowfield behind the capsule. This flow mechanism reasonably explains the features observed in the present numerical simulation, as well as the experimental fact that the dynamic instability occurs at very low reduced frequencies.

Nomenclature

c = speed of sound
D = diameter of the capsule
f = frequency of the oscillation
k = reduced frequency
L = characteristic length
U_∞ = uniform velocity
u = characteristic velocity
X = axial coordinate
x_t, y_t, z_t = velocity components of the grid
θ = pitch angle
$\theta_{\max}$ = amplitude of the oscillation
ω = angular velocity, $2\pi f$

Introduction

THE exploration of asteroids has been a challenging topic from both scientific and engineering sides. The Institute of Space and Astronautical Science started the asteroid sample-return project Muses-C in 1995[1] aiming at launch in 2002 and rendezvous with the asteroid Nereus in 2004. The collected sample will be returned by the reentry capsule separated from the mother spacecraft in 2006. The reentry capsule is planned to reenter directly from the hyperbolic Earth-return trajectory to save the fuel required to transfer the orbit.[1] Consequently, the nominal reentry velocity is expected to be 12 km/s, which is much higher than that for the reentry from the Earth's orbit, and severe heating is expected. Lowering the ballistic coefficient reduces the convective heating in general; therefore, the ballistic coefficient of the capsule has to be made as small as possible.

Figure 1 shows the preliminary design of the reentry capsule. The large nose radius produces large drag, and the short body length reduces the total weight, resulting in a small ballistic coefficient.

In addition to heat protection, attitude control of the capsule is an important issue in the development of reentry capsules. To protect the payload from strong heating in the hypersonic region and to ensure the deployment of the parachute in the transonic region, the attitude of the vehicle must be maintained within the limit in the whole speed range. Because the capsule (Fig. 1) does not have an active attitude control device, the attitude of the capsule must be maintained by its own aerodynamic stability, and therefore aerodynamic stability of the capsule is important for its design. Most of the basic configuration parameters such as nose radii or body lengths are determined mainly from the thermal protection requirement, and there are little room to optimize the configuration with respect to the aerodynamic stability. Fortunately, the center of gravity of such an capsule is located in forward of the center of pressure, and the object is statically stable. However, methods to evaluate the dynamic stability of a capsule are not established, and self-exited pitching oscillation of the reentry capsule in the transonic region was observed in the experiment.[2] This instability phenomenon has been known and experimentally studied since the 1960s.

Dynamic instability was reported in the development of the Gemini capsule,[3] but the length of the Gemini capsule was longer than that of the capsule considered in this study, and the incidence range that the instability was observed was very small. In the Viking project, the shape of the capsule was similar to the Muses-C capsule, and the capsule was found to be dynamically unstable at the angle of attack between −8 and 8 deg (Ref. 4). Yoshinaga[5] carried out the single-degree-of-freedom wind-tunnel test for the OREX reentry capsule and compared the result with the flight data. Hiraki et al.[6] measured the unsteady surface pressure of the oscillating capsule and found that the base pressure was responsible for the dynamic instability. Berner and Winchenbach[7] and Chapman and Yates[8] measured the aerodynamic characteristics of various blunt capsules using a ballistic range test facility.

Despite these studies, the detailed mechanism of dynamic instability at transonic speeds is not well understood. The purpose of the present study is to reveal the mechanism of dynamic instability.

Method of Analysis

One of the characteristic features of the instability phenomena observed in the Hiraki et al. experiment[6] was that the reduced frequency of the limit-cycle oscillation given by

$$k = 2\pi f D / U_\infty$$

is as low as 0.03, which is one order of magnitude lower than those of other dynamic instability phenomena such as flutter. In the normal sense, the flowfield is considered to be quasi steady and dynamic instability is rarely expected at the reduced frequency of 0.03.

The fact that dynamic instability occurred even at the very low reduced frequency indicates that the true reduced frequency is one order larger than the apparent reduced frequency defined by the preceding equation. In other words, the length scale of the phenomena may be larger than the size of the object, and/or the characteristic speed may be slower than the uniform velocity.

If the length scale of the phenomena is larger than the size of the object, the key phenomena that dominates the instability possibly

---

Presented as Paper 98-4451 at the AIAA Atmosphere Flight Mechanics Conference, Boston, MA, 10–12 August 1998; received 4 June 1999; revision received 10 August 2000; accepted for publication 20 September 2000.

*Research Associate, High Speed Aerodynamics, Yoshinodai 3-1-1; teramoto@flab.eng.isas. ac.jp. Member AIAA.

†Research Associate, Safety Engineering, Yoshinodai 3-1-1. Member AIAA.

‡Professor, High Speed Aerodynamics, Yoshinodai 3-1-1. Associate Fellow AIAA.

Table 1 Capsule geometry

Property	Value
Nose radius	50 mm
Semi-apex angle	45 deg
Maximum diameter	100 mm
Body length	50 mm
Base configuration	45-deg truncated cone

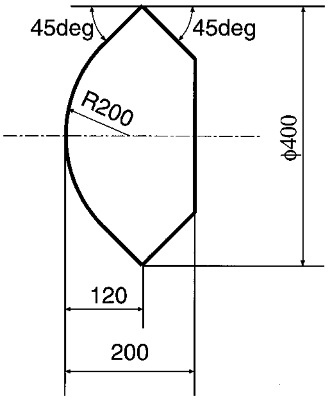

Fig. 1 Reentry capsule of the Muses-C.

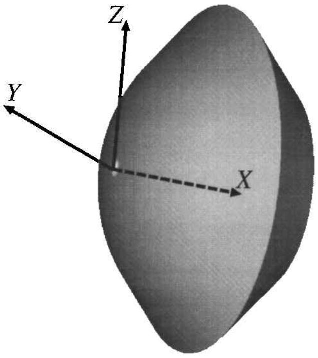

Fig. 2 Model capsule and coordinate systems.

occurs at the region away from the body. Therefore, the flowfield away from the body has to be discussed for the analysis of the instability mechanism.

From this viewpoint, we have chosen the computational approach that gives us the time-dependent information of the whole flowfield.

Figure 2 shows the capsule used in the present simulation. It is same as the capsule used in Hiraki's experiment. The geometry of the capsule is given in Table 1.

Hiraki's experiment was carried out with the one-dimensional free oscillation method. The flowfield during the transition to the limit cycle was discussed, as well as the flowfield in the limit cycle. It took about 20 cycles to reach the limit cycle, and the limit-cycle oscillation observed in the experiment[6] was almost sinusoidal. Therefore, the motion of the capsule was approximated by the forced sinusoidal oscillation. Only the flowfield in the limit cycle is discussed in the present simulation.

Numerical Method

The governing equations are the Reynolds averaged unsteady three-dimensional thin-layer Navier–Stokes equations formulated in the moving grid system:

$$\partial_t \hat{Q} + \partial_\xi \hat{E} + \partial_\eta \hat{F} + \partial_\zeta \hat{G} = \partial_\zeta \hat{S}_V$$

Length, density, and velocity are normalized by the diameter of the capsule, density, and the speed of sound at the far field, respectively.

The grid rotates about its y axis (Fig. 2) sinusoidally, and the velocity at each grid point is given by

$$x_t = z\theta_{\max}\omega\cos(\omega t), \qquad y_t = 0, \qquad z_t = -x\theta_{\max}\omega\cos(\omega t)$$

Because the grid rotates with the capsule, the coordinate and the metrics are evaluated at every time step.

Table 2 Flow condition

Parameter	Value
Mach number	1.3
Diameter of capsule	0.1 m
Reynolds number	2.5×10^6
Frequency	20 Hz
Maximum pitch angle	±20 deg
Reduced frequency	0.03

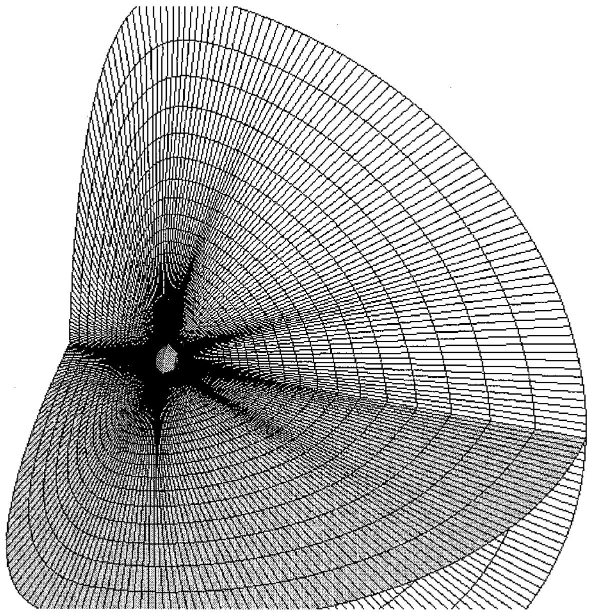

Fig. 3 Computational grid.

The numerical fluxes for the convective terms are evaluated by the simple high-resolution upwind (SHUS)[9] scheme and is extended to higher order by the MUSCL interpolation based on the primitive variables. The SHUS scheme is a family of the AUSM-type scheme that was developed by Shima and Jounouchi.[9] Experience has shown that it is more robust and efficient than Roe's flux difference splitting.

The lower–upper alternating direction implicit (LU–ADI) factorization implicit algorithm[10] with no inner iterations is used for the time integration. The flowfield is considered to be fully turbulent, and Baldwin–Lomax's algebraic turbulence model[11] is used. There has been a lot of discussion about the use of zero-equation turbulence models for unsteady flow simulations. However, the separation point is obviously fixed to the edge of the capsule for this case, and the turbulence model does not seem to influence the qualitative mechanism of the flowfield. Therefore, one of the simplest turbulence models was used to reduce the computational cost.

The computational grid is shown in Fig. 3. The grid consists of $121 \times 64 \times 81$ points. The minimum grid spacing at the wall is 6.0×10^{-5} in nondimensional units. The wall coordinate y^+ at the first grid point is less than 5 over most of the surface. At least one grid point is distributed inside the laminar sublayer. The computational domain ranges from -2.0 to 10.0 in the x direction and -10.0 to 10.0 in the y and z directions. The finer grid ($151 \times 64 \times 121$) and the coarser grid ($121 \times 64 \times 41$) are also used for discussion of the grid sensitivity.

Table 2 shows the flow conditions to be computed. They correspond to those of the wind-tunnel experiment.[6] One oscillation cycle corresponds to approximately 150 in nondimensional time, and the time step Δt is set to be 1/150,000 of the cycle. The maximum Courant–Friedrichs–Lewy number is about 30 at the wall.

The simulation was started from the steady-state solution at 0-deg angle of attack. During the computation, overall aerodynamic forces are monitored. The histories of the forces at the third cycle are consistent with those at the second cycle, and the flowfield is considered to have reached the periodic cycle in two cycles. The computation

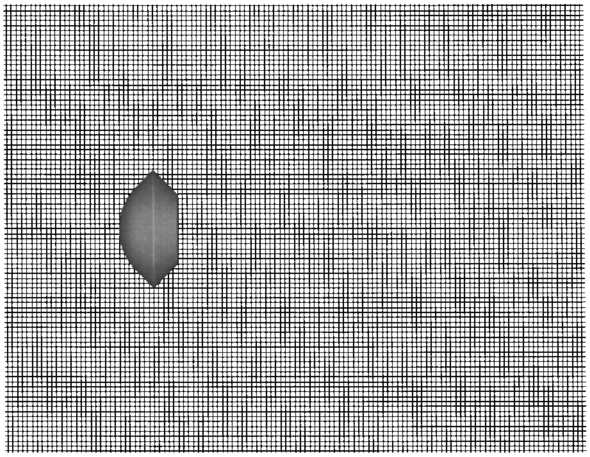

Fig. 4 Grid for postprocessing.

required 40 h on 4 PE Fujitsu VPP500 for the simulation of one oscillation cycle. A total of seven cycles were simulated after the flow reached the periodic state.

Data Processing

Instantaneous physical properties of the flowfield were saved to files every 1000 time steps, and 150 data files (1.3 GB in size) were created each cycle. These properties were defined on the moving grid fixed to the capsule and are inconvenient for the analysis. Therefore, the properties were mapped over the equally spaced rectangular grid shown in Fig. 4. The rectangular grid is fixed to the space, and time series of data are obtained at each point. The time series of data were then processed by Fourier analysis, and spatial distribution of amplitude and phase were obtained.

The spatial distribution of the phase is closely related to the speed of propagation. Suppose that the disturbance is transferred by the acoustic waves, the time required for the propagation to a point downstream is x/c, and the phase at the point would be delayed $2\pi f x/c$, where c is the speed of the wave, x is the distance to the point, and f is the frequency of the wave. Therefore, the spatial gradient of the phase caused by the propagation becomes $2\pi f/c$ (rad/m).

The relation between the speed of the propagation and the spatial gradient of the phase will be used in the following discussions.

Results

Overview of the Flowfield

Figure 5 shows the instantaneous density gradient distributions around the capsule. Characteristic features of the flowfield around a blunt body at supersonic speeds, such as the bow shock wave ahead of the capsule, the wake, and the recompression shock waves emanating from the neck point, are observed. These essential features do not change even when the capsule oscillates, although their locations move with the capsule.

At the moment shown in Fig. 5, the pitch angle of the capsule is 0, the capsule is in pitch-up motion, and the wake moves upward. In Fig. 5, the wake is located below the centerline while the capsule is in the neutral position. It shows that the motion of the wake is delayed from that of the capsule. Also the recompression shock waves above and below the wake are not symmetric. On the other hand, the bow shock wave in front of the capsule is symmetric, and it moves synchronously with the capsule.

In the spectrum diagram of the lift coefficient shown in Fig. 6, there are several peaks near the frequency of the capsule's oscillation (20 Hz), and other peaks appear near 1 kHz, which corresponds to the frequency of vortex shedding behind the capsule. The shed vortex is convected downstream, and it makes the wake highly unsteady. The frequency of the capsule's oscillation is far lower than that of the vortex shedding, and it seems that the vortex shedding does not directly contribute to the dynamic instability of the capsule.

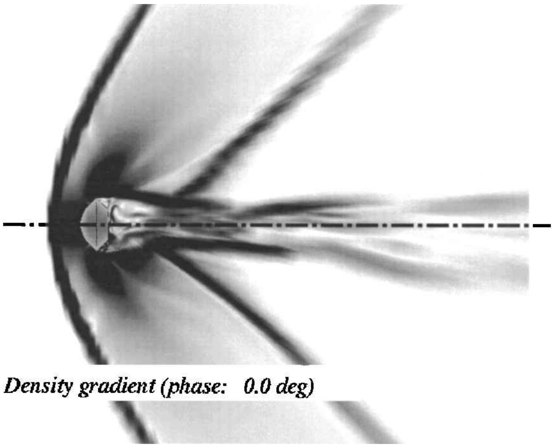

Fig. 5 Instantaneous density gradient distribution.

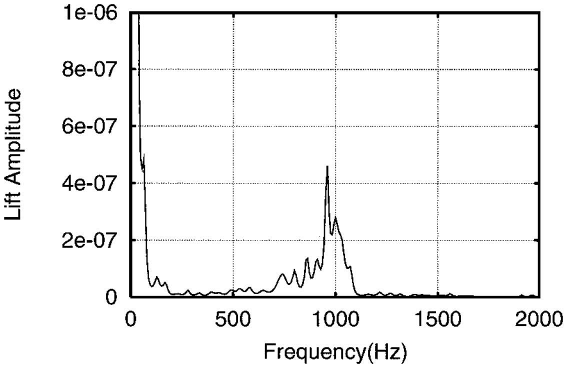

Fig. 6 Power spectrum density of the fluctuation of C_L.

Grid Sensitivity Study

Figures 7–9 compare the flowfields obtained with three different grid resolutions. The upper halves of Figs. 7–9 show the contour lines of the density gradient, and the lower halves show the grid distributions. The fine grid ($151 \times 64 \times 121$) clearly resolves the flow features such as the bow shock wave, the wake, and the recompression shock wave. The base grid ($121 \times 64 \times 81$) still resolves these flow features and the position of the shock waves are the same as those of the fine grid, but, as the grid becomes further coarser ($121 \times 64 \times 41$), the recompression shock wave moves forward and merges with the wake. The histories of the base pressure shown in Figs. 10–12 show the same tendency. The histories obtained from the fine grid and the base grid show the hysteresis at all of the angles between -20 and 20 deg, whereas the history obtained from the coarse grid shows the hysteresis only at small angle of attack.

Note that the reduced frequency of the capsule's oscillation is as low as $\mathcal{O}(0.01)$. The length scale of the flow structure corresponding to the harmonic oscillation should be in the same order as the diameter of the capsule. The base grid resolves the flow structures that have length scale comparable with the diameter of the capsule, and it gives the same history of the surface pressure as the fine grid. The solution with the base grid is used for the discussion in the current study.

Discussion

Pitching Moment and Surface Pressure

The aerodynamic pitching moment around the axis of rotation is plotted against the pitch angle in Fig. 13. The gradient of the moment $\partial M/\partial\theta$ is negative, and the aerodynamic moment works to suppress the pitch angle of the capsule. Therefore, the capsule is statically stable.

Hysteresis of the moment is also observed from Fig. 13. The pitching moment is higher when the angular velocity is positive than when the angular velocity is negative. Consequently, net work input to the capsule during one oscillation cycle is positive, and the amplitude of the oscillation grows. Thus, the capsule is

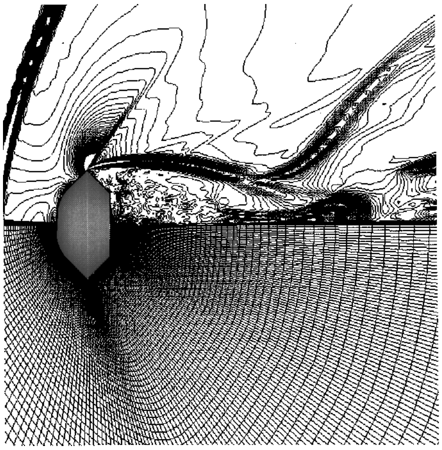

Fig. 7 Density gradient distribution: fine grid, 151 × 64 × 121.

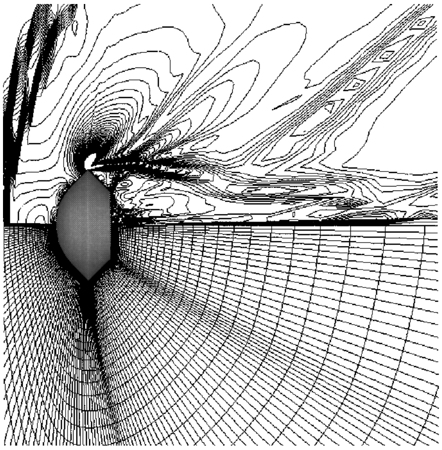

Fig. 8 Density gradient distribution: base grid, 121 × 64 × 81.

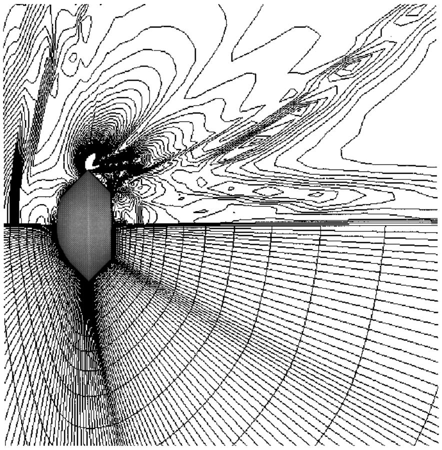

Fig. 9 Density gradient distribution: coarse grid, 121 × 64 × 41.

dynamically unstable under this enforced oscillation while it is statically stable.

Time histories of the surface pressure at one spot in the front and at another spot in the base parts of the capsule (both spots are in the plane of symmetry, and their positions are shown in Fig. 14) are plotted with the history of the pitch angle in Fig. 15. The crosses in Fig. 15 denotes the instantaneous surface pressure obtained by the numerical simulation, and the dashed lines are the curve-fit result from the Fourier analysis.

The surface pressure at the front spot varies synchronously with the pitch angle; the pressure is the same at the same pitching angle

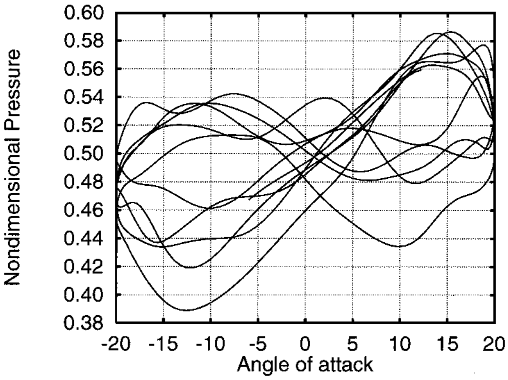

Fig. 10 History of the surface pressure: fine grid, 151 × 64 × 121.

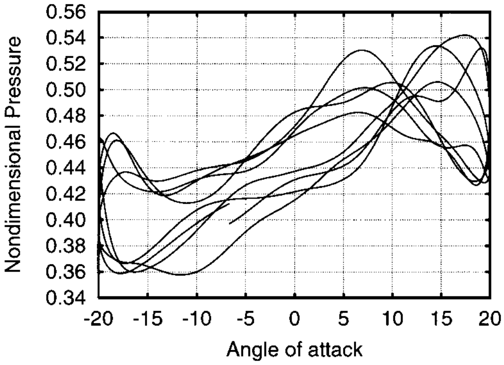

Fig. 11 History of the surface pressure: base grid, 121 × 64 × 81.

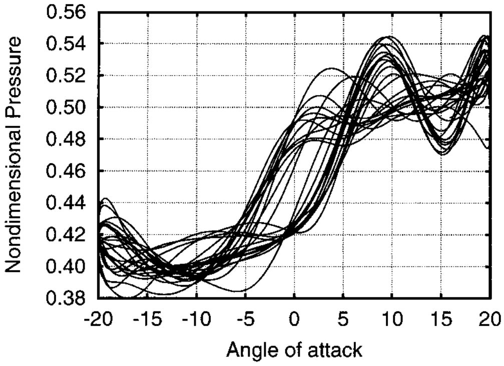

Fig. 12 History of the surface pressure: coarse grid, 121 × 64 × 41.

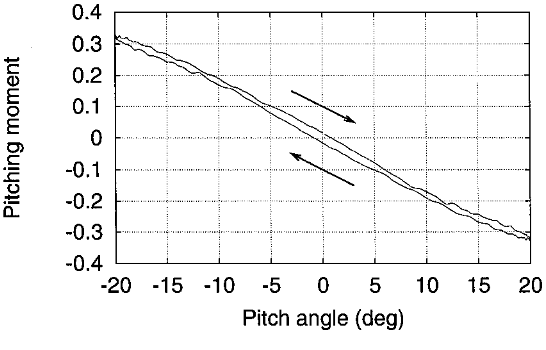

Fig. 13 History of the overall aerodynamic pitching moment.

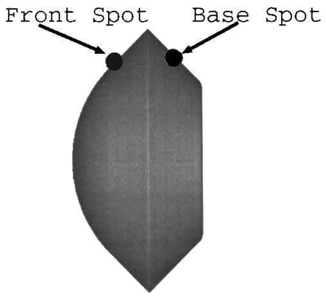

Fig. 14 Pressure tap locations.

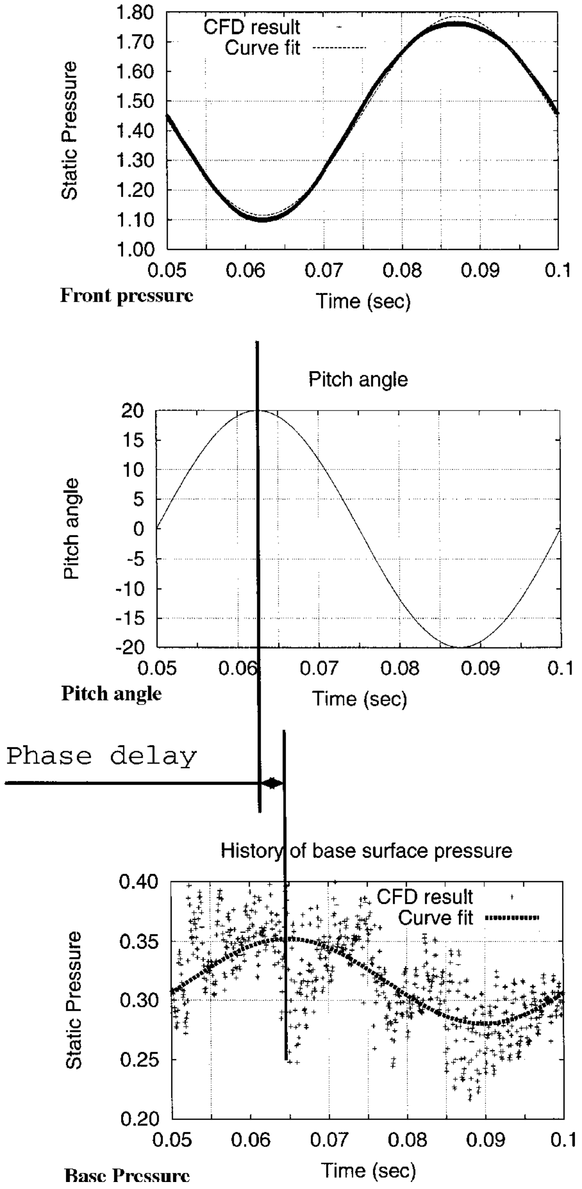

Fig. 15 History of the surface pressure.

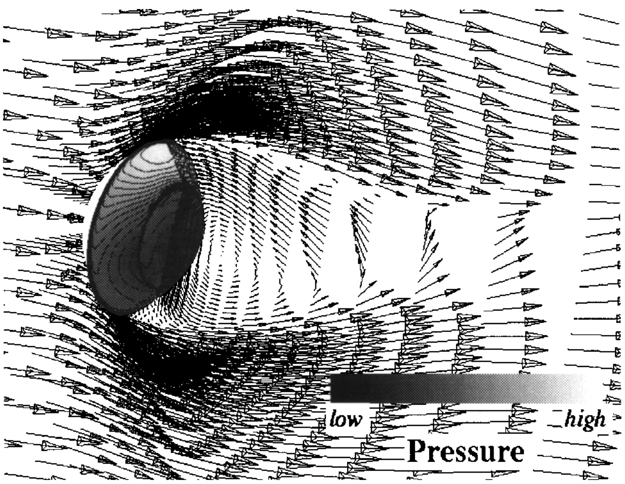

Fig. 16 Base pressure distribution and velocity field behind the capsule.

in both pitching up and pitching down. Therefore, the front pressure does not contribute to the hysteresis of the pitching moment. On the other hand, phase delay is observed in the base pressure plots. The base pressure at a certain pitch angle varies depending on the direction of the pitching motion, and hence, the pitching moment due to the base pressure shows hysteresis.

The upper part of the base pressure increases when the pitch angle is positive, and the positive static pressure at the rear spot acts to rotate the capsule toward the pitching-down direction. Therefore, the phase delay of the rear pressure makes the net work input positive, and makes the capsule dynamically unstable. The delay time is approximately 2.1 ms, which corresponds to 15 deg in the phase angle.

From the preceding discussion, the dynamic instability of the capsule is caused by the hysteresis of the pitching moment, and it is the phase delay of the backside pressure that produces the hysteresis.

Phase of the Pressure

Because the backside pressure varies in accordance with the pitch angle, there has to be some mechanism that links the oscillation of the capsule and the backside pressure; that is, the disturbance caused by the pitching motion somehow propagates to the base region. The time required for the propagation is considered to be responsible for the phase delay, and therefore the discussion of the correlation between the pitch angle and the backside pressure will help understanding the mechanism of the phase delay.

Figure 16 shows the backside pressure distribution and the velocity field near the capsule at 10-deg angle of attack. The flowfield around the capsule is divided into regions inside and outside of the recirculation, and two regions are separated by the shear layer. The flowfield outside of the recirculation is directly linked with the attitude of the capsule. Considering the size of the capsule ($D = 0.1$ m), the flowfield varies almost instantaneously (less than 1 ms) when the capsule changes its pitch angle. On the other hand, the flowfield inside the recirculation region is not directly influenced by the capsule's pitch angle, and the variation of the flowfield may be delayed from the pitch angle. The amount of the delay time depends on the mechanism that links the pitch angle and the flowfield. The mechanism is not evident, but there are two possible mechanisms.

The first is that the backside pressure is influenced directly by the pressure outside the region of phase delay; the backside pressure is determined to match with that of the outside region. If this were the case, the disturbance caused by the pitching motion would propagate with the acoustic waves and the pressure phase angle should vary continuously at the boundary of two regions.

The second is that the backside pressure is determined by the isolated flow structure inside the region of phase delay. If this were the case, the pressures inside and outside the region would be determined from the different mechanism, and there may be discontinuity of the pressure phase at some boundary.

The spatial distributions of the phase angle of the pressure are shown in Fig. 17, and the pressure phase along the dashed lines A and B in Fig. 17 are plotted in Figs. 18 and 19. Contour lines of the density gradient are plotted in the bottom half of Fig. 17 for reference. In Fig. 17, only the region where the pressure phase angle is between −20 and 20 deg is shown, and the white region indicates the area where the phase is delayed. Figure 17 signifies that the pressure phase is delayed only in the recirculating region bounded by the capsule, wake, and the recompression shock wave.

Suppose that the base pressure is directly linked with the pressure outside of the region and the disturbance is transferred by the

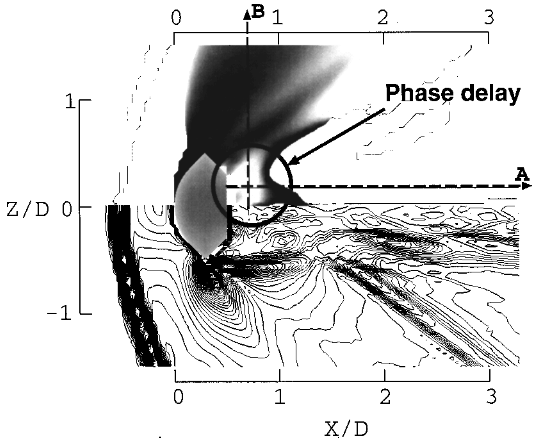

Fig. 17 Pressure phase distribution (top) and density gradient distribution (bottom).

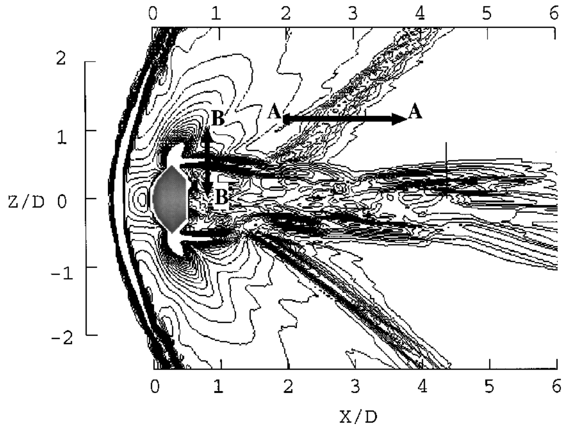

Fig. 20 Oscillation of the shock wave and the wake.

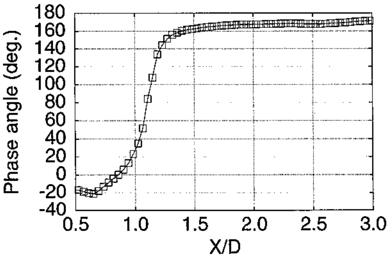

Fig. 18 Pressure phase along line A.

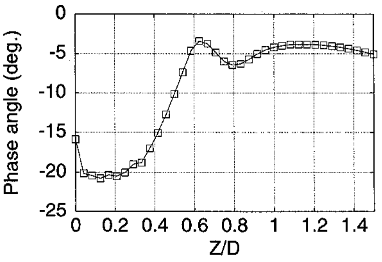

Fig. 19 Pressure phase along line B.

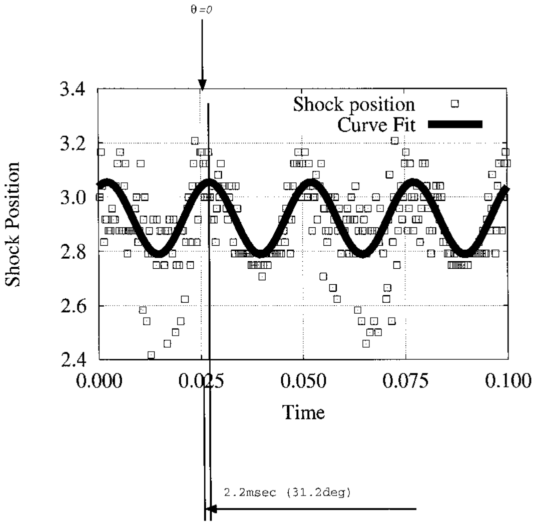

Fig. 21 Shock position along A–A.

acoustic waves; then the spatial gradient of the phase caused by the propagation should be $(2\pi f/c) \simeq 0.4$ (rad/m).

However, the actual spatial phase gradients at the boundaries of the recirculating region are 200 (rad/m) along line A and 14 (rad/m) along line B. Both of them are far larger than 0.4 (rad/m). Therefore, the phase delay of the base pressure can not be the result of the acoustic wave propagation. The base pressure is considered to be independent from the pressure field outside the region and to be determined by the flow structure inside the recirculating region itself.

One of the parameters that characterizes the flow structure inside the recirculating region is the shape of its boundary. Hence, the motion of the boundaries of the recirculating region is discussed in the following sections.

Motion of the Boundaries

The boundaries of the recirculating region are the wake and the recompression shock wave, as shown in Fig. 17.

The section B–B corresponds to the boundary of the recirculating region. Because the position of the capsule's edge moves when the capsule oscillates, the deviation of the edge position is subtracted from that of the wake position. The amplitude and phase of the radial position of the wake along the section B–B in Fig. 20 are 0.016 and −98.40 deg, respectively. The amplitude of the oscillation is less than 2% of the diameter of the capsule, and it seems that the position of the wake near the capsule does not influence the pressure behind the capsule.

The axial location of the recompression shock wave along the section A–A in Fig. 20 is plotted against the time in Fig. 21. The recompression shock wave oscillates twice during one cycle of the oscillation of the capsule (0.05 s). The recompression shock wave takes its most backward position 2.2 ms after the capsule reaches the neutral (pitch angle $\theta = 0$) position. Thus, the unsteady motion of the recompression shock wave is 2.2 ms delayed from the capsule.

The delay time coincides with that of the static pressure behind the capsule, and it seems that the phase delay of the base pressure is associated with the motion of the recompression shock wave.

Interaction Between the Recompression Shock Wave and the Wake

The recompression shock wave is a compression wave caused by the interaction with the wake. Therefore, the motion of the recompression shock wave is considered to be determined by the interaction with the wake.

The amplitude of the pressure oscillation is shown in the top half of Fig. 22, and the phase of the pressure oscillation is shown in the bottom. A region of high-pressure amplitude is observed near the centerline between $X/D = 1.5$ and 4.0. The amplitude is the maximum near the foot of the recompression shock wave $X/D = 2.0$, and diminishes as it goes downstream. The amplitude is almost zero downstream of $X/D = 4.0$. It seems that the interaction between the wake and the recompression shock wave takes place in the region between $X/D = 2.0$ and 4.0 for the most part.

The pressure phase angle at the region is almost constant, and it is approximately −16 deg. The delay time coincides with that of the recompression shock wave. Therefore, not only the wake's motion at the foot of the recompression shock wave, but all of the wake's motion between $X/D = 2.0$ and 4.0 influences the motion of the recompression shock wave.

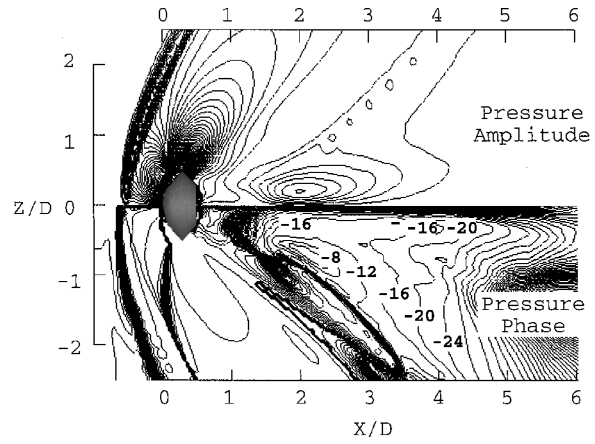

Fig. 22 Pressure amplitude (top) and pressure phase (bottom).

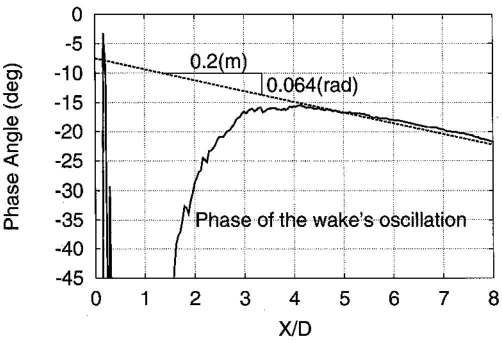

Fig. 23 Phase of the oscillation of the wake.

Oscillation of the Wake

The axial distribution of the phase angle of the vertical location of the wake is shown in Fig. 23 and it is seen that 1) the wake at $X/D = 4.0$ oscillates with 16 deg of phase delay, which is the same delay as that of the recompression shock wave, and 2) the axial gradient of the phase downstream of $X/D = 4.0$ is almost constant at 0.32 rad/m.

The gradient of 0.32 rad/m corresponds to what would be caused by the propagation at uniform velocity. Therefore, the oscillation of the wake propagates simply at the uniform velocity downstream of $X/D = 4.0$. It is also shown in the preceding section that the wake interacts with the recompression shock wave between $X/D = 2.0$ and 4.0. Consequently, the section $X/D = 4.0$ is the rear end of the interaction region, and it seems that the motion of the wake at $X/D = 4.0$ dominates the motion of the recompression shock wave.

The flow mechanism that makes the wake's oscillation at $X/D = 4.0$ delayed 16 deg is not evident from the present simulation. However, if it is assumed that the disturbance due to the oscillation of the capsule propagates at half of the uniform velocity (which is a reasonable convective velocity inside the shear layer) between the capsule and $X/D = 4.0$, it would cause phase delay of 15 deg at $X/D = 4.0$.

Proposed Mechanism of Dynamic Instability

Mechanism of Dynamic Instability

The computed features of the flowfield around the capsule oscillating at transonic speeds can be summarized as follows:

1) The hysteresis of the pitching moment is caused by the delay of the base pressure.

2) The oscillation of the static pressure is delayed only in the recirculating region bounded by the capsule, the wake, and the recompression shock wave. The phase of the pressure in this region seems to be controlled by the motion of the recompression shock wave.

3) The wake interacts with the recompression shock wave at the area between $X/D = 2.0$ and 4.0.

4) The base pressure, recompression shock wave, and the wake at $X/D = 4.0$ oscillate with the same delay time (approximately 2 ms).

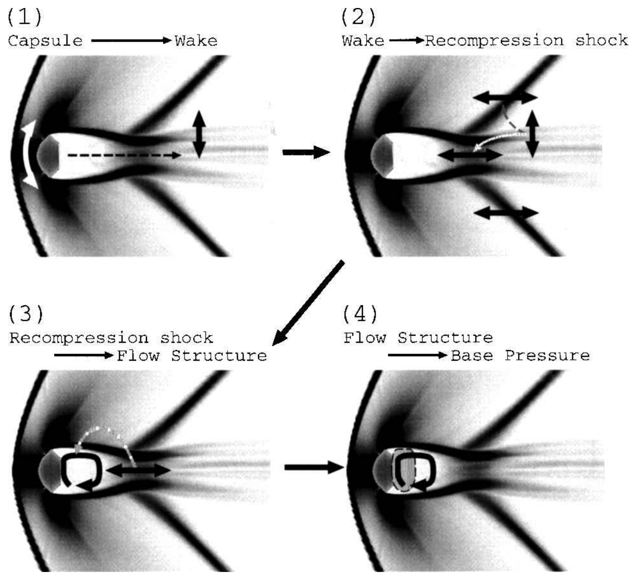

Fig. 24 Proposed mechanism of the dynamic instability.

Fig. 25 Characteristic parameters.

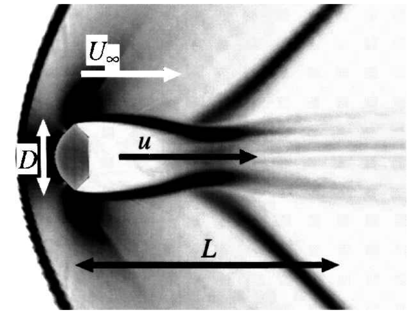

We propose the following flow mechanism to explain these features (see Fig. 24):

1) The disturbance due to the capsule's oscillation is convected downstream inside the wake. The speed of the convection is about half of the uniform velocity. Because the speed of the propagation is finite, the oscillation of the wake downstream is delayed.

2) The motion of the recompression shock wave is influenced by the oscillation of the wake at the rear end of the interaction. Because the oscillation of the wake is delayed, the motion of the recompression shock wave is also delayed.

3) The flow structure inside the recirculating region is influenced by the oscillation of the recompression shock wave. The motion of the recompression shock wave is delayed; consequently, the oscillation of the flow structure is delayed as well.

4) The base pressure is controlled by the flow structure inside the recirculating region. Therefore, the oscillation of the base pressure is delayed.

5) The delay of the base pressure causes hysteresis in the pitching moment, and it make the capsule's oscillation dynamically unstable.

Characteristic Parameter of the Phenomena

When such a mechanism is assumed, the characteristic length L of the phenomenon is considered to be the distance between the capsule and the rear end of the region where the wake interacts with the recompression shock wave. The characteristic speed u is the average speed of the propagation inside the wake. Their values are $4D$ for the characteristic length and $0.5U_\infty$ for the characteristic speed in this case, as shown in Fig. 25.

Thus, true reduced frequency defined from (L, u) is one order larger than the apparent reduced frequency defined from (D, U_∞). The apparent reduced frequency is 0.03, and it is so low that no dynamic instability is likely to occur. On the other hand, true reduced frequency is 0.24, which is a reasonable value for the dynamic instability to occur.

Consequently, dynamic instability may occur even when the apparent reduced frequency is sufficiently small. This mechanism reasonably explains the experimental fact that the dynamic instability is observed at very low reduced frequencies.

Conclusions

The flowfield around a capsule oscillating at a transonic speed was numerically simulated, and the mechanism of the dynamic instability observed in the experiments was revealed. The computed results showed that the dynamic instability is caused by the phase delay of the base pressure.

The flow model that explains the mechanism of the dynamic instability was proposed. The phase delay of the base pressure is created through the feedback loop from the capsule, wake, recompression shock wave and to the base pressure.

The proposed model still has to be examined through further experiments and numerical simulations. However, it reasonably explains the features observed in the present simulation, as well as the experimental fact that the dynamic instability is observed at very low reduced frequencies.

References

[1] Working Group of Asteroid Sample Return Mission, "Asteroid Exploration Plan (Muses-C)," Inst. of Space and Astronautical Science, Sagamihara, Kanagawa, Japan, March 1995 (in Japanese).

[2] Inatani, Y., Ishii, N., and Abe, T., "Design of MUSES-C Capsule," *Symposium on Flight Mechanics and Astrodynamics*, Inst. of Space and Astronautical Science, Kanagawa, Japan, 1996, pp. 1–6 (in Japanese).

[3] Wright, B. R., and Kilgore, R. A., " Aerodynamic Damping and Oscillatory Stability in Pitch and Yaw of Gemini Configurations at Mach Numbers form 0.50 to 4.63," NASA TN D-3334, March 1966.

[4] Sammonds, R. I., and Kruse, R. L., "Viking Entry Vehicle Aerodynamics at $M = 2$ in Air and Some Preliminary Test Data for Flight in CO_2 at $M = 11$," NASA TN D-7974, June 1975.

[5] Yoshinaga, T., Tate, A., Watanabe, M., and Shimoda, T., "Orbital Re-Entry Experiment Vehicle Ground and Flight Dynamic Test Results Comparison," *Journal of Spacecraft and Rockets*, Vol. 33, No. 5, 1996, pp. 635–642.

[6] Hiraki, K., Inatani, Y., Ishii, N., Nakajima, T., and Hinada, M., "Dynamic Stability of MUSES-C Capsule," 21st International Symposium on Space Technology and Science, Rept. ISTS-98-d-33, May 1998.

[7] Berner, C., and Winchenbach, G. L., "Numerical and Experimental Investigation of Generic Space Probes," AIAA Paper 98-0798, Jan. 1998.

[8] Chapman, G. T., and Yates, L. A., "Dynamics of Planetary Probes: Design and Testing Issues," AIAA Paper 98-0797, Jan. 1998.

[9] Shima, E., and Jounouchi, T., "Role of CFD in Aeronautical Engineering (No. 14)—AUSM type Upwind Schemes," *Proceedings of the 14th NAL Symposium on Aircraft Computational Aerodynamics*, National Aerospace Lab., Tokyo, 1997, pp. 7–12.

[10] Obayashi, S., and Matsushima, K., and Fujii, K., and Kuwahara, K., "Improvements in Efficiency and Reliability for Navier–Stokes Computations Using the LU-ADI Factorization Algorithm," AIAA Paper 86-0338, Jan. 1986.

[11] Baldwin, B. S., and Lomax, H., "Thin Layer Approximation and Algebraic Model for Turbulent Flows," AIAA Paper 78-257, Jan. 1978.

S. K. Aggarwal
Associate Editor